Original Paper

Tuning active sites in MoS_2-based catalysts via H_2O_2 etching to enhance hydrodesulfurization performance

Shui-Sen He [a], Ting-Ting Huang [b], Chao Chen [a], Yu Fan [a, *]

[a] *State Key Laboratory of Heavy Oil Processing, China University of Petroleum, Beijing, 102249, China*
[b] *State Key Laboratory Base for Eco-Chemical Engineering in College of Chemical Engineering, Qingdao University of Science and Technology, Zhengzhou Road 53, Qingdao, 266042, Shandong, China*

A B S T R A C T

A H_2O_2 etching strategy was adopted to introduce coordinatively unsaturated sites (CUS) on MoS_2-based catalysts for dibenzothiophene (DBT) hydrodesulfurization (HDS). The CUS concentrations on MoS_2 slabs were finely regulated by changing the concentrations of H_2O_2 solution. With the increasing H_2O_2 concentrations (0.1—0.3 mol/L), The CUS concentrations on MoS_2 slabs increased gradually. However, the high-concentration H_2O_2 etching (0.5 mol/L) increased the MoO_xS_y and MoO_3 contents on MoS_2 slabs compared to etching with the H_2O_2 concentration of 0.3 mol/L, which led to the less CUS concentration in the sulfided Mo−H-0.5 catalyst than in the sulfided Mo−H-0.3 catalyst. A microstructure-activity correlation indicated that the CUS introduced by H_2O_2 etching on MoS_2 slabs significantly enhanced DBT HDS. Different Co loadings were further introduced into Mo−H-0.3, which had the most CUS concentration, and the corresponding 0.2-CoMo catalyst with the highest CoMoS content (3.853 wt%) exhibited the highest reaction rate constant of 6.95×10^{-6} mol g^{-1} s^{-1} among these CoMo catalysts.

1. Introduction

With currently strict environmental standards and an apparent increase in heavy crude oil use, the key to achieving ultraclean fuel production is to refine the heavy crude oil into gasoline and diesel with sulfur contents less than 10 ppm (Yuan et al., 2020; Asadi et al., 2019; Wang et al., 2017). Hydrodesulfurization (HDS) is commonly used to remove the sulfur compounds from fuel. Conventional HDS catalysts are composed of transition metal sulfides (TMS), including Mo(W) as the active component and Co(Ni) as the promoter, and Al_2O_3 serves as the support (Brunet et al., 2005). However, the HDS activities of alumina-based catalysts loaded with active metals are restricted by the low density of HDS active sites and the poor structures of active phases caused by strong metal-support interactions (Zhou et al., 2017). To deepen the understanding of the relationships between active microstructures and their HDS activities, bulk Co(Ni)−Mo(W) HDS catalysts were studied extensively (Varakin et al., 2018; Li et al., 2014; Afanasiev, 2010).

Recently, graphene-like structures of TMS, such as two-dimensional (2D) MoS_2, have attracted widespread attention, and various nanostructures have been reported for MoS_2. Lai et al. (2016) synthesized homogeneous NiMoS nanoflowers with self-assembled nanosheets by a hydrothermal growth method using sulfur as the sulfur source. Cao et al. (2020) prepared defect-rich 1T-2H MoS_2 nanoflowers via a solvothermal method using water, ethanol and glycerol. Abbasi et al. (2020) successfully synthesized bulk MoS_2 and cobalt-loaded MoS_2 nanosheets using molybdenum oxide and thiourea under an inert gas and at high temperature. However, the low concentrations of active S vacancies in the synthesized MoS_2 nanoparticles described above resulted in inferior HDS activities. De la Rosa et al. (2004) attempted to separate TMS particles from the Al_2O_3 support with HF etching to eliminate the support disturbance. Nevertheless, for CoMoS catalysts, etching of the support with HF led to Co loss and rearrangement of MoS_2 particles, which partially destroyed the structures of CoMoS active phases and reduced the dibenzothiophene (DBT) HDS activities of the corresponding catalysts (Berhault et al., 2008). In general, unmodified Co(Ni)−MoS_2 particles, as well as Co(Ni)−MoS_2 particles etched with strong corrosive agents, exhibited low activities in HDS of sulfur-containing compounds.

Vacancies constitute crystal point defects and are beneficial in

* Corresponding author.
E-mail address: fanyu@cup.edu.cn (Y. Fan).

regulating the crystal electronic structure and the degree of active site exposure, thus significantly improving the reaction performance of catalysts (Feng et al., 2015; Xiong et al., 2017). Zhang et al. (2019) applied H_2O_2 solutions to etch monolayer MoS_2 slabs and their results showed that when monolayer MoS_2 slabs were exposed to H_2O_2 solutions, the S atoms near the vacancies were first oxidized and replaced by O atoms. Li et al. (2020) found that multilayer MoS_2 was partially dissolved into monolayer MoS_2 after being mixed with H_2O_2 solutions, which led to a 2H-to-1T phase change of the MoS_2 and thereby promoted the formation of S vacancies. Electron-rich $1T-MoS_2$ exhibited high activity for advanced oxidation processes. No reports have yet been published on applications of H_2O_2-etched MoS_2 slabs for HDS of sulfur-containing compounds, and the relationship between coordinatively unsaturated site (CUS) concentrations on the etched MoS_2 slabs and their HDS performance remains unknown.

Herein, the mild etching agent H_2O_2 was used to etch synthesized three-dimensional MoS_2 nanoflowers in an effort to accurately regulate the quantity of HDS active sites. Different loading amounts of the promoter Co were introduced into etched MoS_2 to further optimize the number of HDS active sites. The present work finely modulated the CUS concentrations on MoS_2 slabs by changing the concentrations of H_2O_2 solution. Then, the Co loading amounts of the Mo−H-0.3 catalyst with the highest CUS concentration were further adjusted to obtain the optimal HDS catalyst.

2. Experimental

2.1. Materials

Sodium molybdate dihydrate ($Na_2MoO_4 \cdot 2H_2O$, 99.0%), thioacetamide (CH_3CSNH_2, 99.0%), acetic acid (CH_3COOH, 99.5%), hydrogen peroxide solution (H_2O_2, 37.0%), cobalt nitrate hexahydrate ($Co(NO_3)_2 \cdot 6H_2O$, 99.0%), n-heptane (C_7H_{16}, 98.0%), ethanol (C_2H_5OH, 99.5%), decahydronaphthalene ($C_{10}H_{18}$, 99.0%), dibenzothiophene (DBT, 99.0%), and carbon disulfide (CS_2, 99.9%) were purchased from Shanghai Aladdin Company (China).

2.2. Preparation of catalysts

In the synthetic process, 1.5 g of $Na_2MoO_4 \cdot 2H_2O$ was solubilized in 70 mL of deionized water and magnetically stirred for 15 min at 25 °C. Then, 0.94 g of CH_3CSNH_2 was dispersed in the above solution. Subsequently, the pH of the resulting mixture was changed to 4.0 with acetic acid. After stirring for 40 min, the clarified blue-green solution was transferred into a 100 mL stainless steel Teflon-lined autoclave, which was maintained at 200 °C for 20 h. The resulting black precipitate was filtered, and thoroughly washed with 500 mL of deionized water and ethanol absolute. Finally, the obtained catalyst was dried in a vacuum oven at 80 °C for 12 h and abbreviated as Mo−H-0.

A total of 1.5 g of the MoS_2 powder obtained in the above-mentioned process was dispersed in H_2O_2 solutions with variable concentrations (0.1, 0.2, 0.3 and 0.5 mol/L) and stirred at high speed for 5 min at 25 °C. The etched samples were filtered, washed and dried in a vacuum oven at 80 °C for 12 h. The collected catalysts were abbreviated as Mo−H-x (where x = 0.1, 0.2, 0.3 and 0.5).

Cobalt species were introduced into the aforementioned Mo−H-3.0 by incipient wetness impregnation using cobalt nitrate hexahydrate as the cobalt precursor with Co/(Co + Mo) ratios of 0.05, 0.1, 0.2 and 0.3. Then, the impregnated catalysts were dried in a vacuum oven at 80 °C for 12 h. The collected catalysts were abbreviated as x-CoMo (where x = 0.05, 0.1, 0.2 and 0.3).

2.3. Characterization techniques

X-ray diffraction (XRD) patterns were recorded with a Bruker D8 focus diffractometer equipped with a Cu $K\alpha$ emission over the $5 \leq 2\theta \leq 90°$ range with a scanning speed of 4 °/min. Physical N_2 adsorption-desorption measurements were performed on a Quantachrome adsorption instrument from the Conta Instrument Company. Scanning Electron Microscopy (SEM) images were performed on a HITACHI SU8010 instrument operated at an accelerating voltage of 20 kV. Raman spectra of the catalysts were collected on a LabRAM Aramis spectrometer ($\lambda = 532$ nm) over the range $100-1600$ cm^{-1}. Electron paramagnetic resonance (EPR) spectra were obtained at 9.846 GHz by using a Bruker A200 spectrometer at 100 K.

Temperature-programmed reduction (TPR) studies of the catalysts were carried out with an AutoChem1 II 2920 instrument. 0.1 g of catalyst was placed in U-shape quartz tube and pretreated under He flow from room temperature to 150 °C at a rate of 10 °C/min for 1 h. After the baseline was stabilized, the catalyst was heated at a rate of 10 °C/min to 800 °C in a mixture of 10% H_2/Ar (50 mL/min). The amount of hydrogen consumed was detected by TCD detector.

The images of the catalysts were characterized by a High-resolution transmission electron microscopy (HRTEM) operated with 200 kV accelerating voltage (Tecnai G2 F20). The average lengths ($\overline{L}$) and stacking numbers ($\overline{N}$) of the MoS_2 slabs were obtained by analyzing 20 representatives HRTEM micrographs (at least 500 crystallites) as follows (Kasztelan et al., 1984; Song et al., 2018; Chowdari et al., 2021):

$$\overline{L} = \frac{\sum_{i=1}^{n} x_i L_i}{\sum_{i=1}^{n} x_i} \text{ and } \overline{N} = \frac{\sum_{i=1}^{n} x_i N_i}{\sum_{i=1}^{n} x_i} \qquad (1)$$

where L_i is the length of slab i, N_i is the stacking degree of slab i, x_i is the number of MoS_2 slabs with L_i length or N_i layers and n is the total number of MoS_2 slabs.

Dispersion of the MoS_2 (D) was statistically evaluated by the following equation:

$$D = \frac{\sum_{i=1}^{t} (6n_i - 6)}{\sum_{i=1}^{t} \left(3n_i^2 - 3n_i + 1\right)} \qquad (2)$$

where n_i denotes the number of Mo atoms along one side the of MoS_2 slab determined by its length ($L = 3.2(2n_i-1)$ Å), and t denotes the total number of MoS_2 slabs.

The chemical structures of the catalysts were analyzed by X-ray photoelectron spectroscopy (XPS) using a PHI 5300 X-ray photoelectron spectrometer with a monochromatic Al $K\alpha$ source provided by Pekinelmer Physics Electronics company. All binding energies of the peaks were calibrated by the C 1s peak at 284.6 eV. The recorded spectra were deconvoluted with PeakFit v4.12 software with a Shirley background subtraction.

The concentration of species j on the catalyst surface was calculated in wt% with the following formula (Pimerzin et al., 2017; Nikulshin et al., 2014):

$$C(j)_T = \frac{(Ar_j \cdot A_j/S_i)}{\sum_{j=1}^{n} (Ar_j \cdot A_j/S_i)} \times 100 \qquad (3)$$

where A_j and Ar_j refer to the peak areas and atomic weight of

species j, respectively. S_j is the sensitivity factor of the species j.

The relative contents of the Co_9S_8 and CoMoS phases were given with the following equations (Pimerzin et al., 2017; Nikulshin et al., 2014):

$$[Co_9S_8] = \frac{A_{Co_9S_8}}{A_{CoMoS} + A_{Co_9S_8} + A_{CoO}} \times 100 \tag{4}$$

$$[CoMoS] = \frac{A_{CoMoS}}{A_{CoMoS} + A_{Co_9S_8} + A_{CoO}} \times 100 \tag{5}$$

where A_x is the fitted peak area of species x.

The effective contents of Co_9S_8 and CoMoS phases were determined in accordance with the following equations (Pimerzin et al., 2017; Nikulshin et al., 2014):

$$C(Co_9S_8) = [Co_9S_8] \times C(Co)_T \tag{6}$$

$$C(CoMoS) = [CoMoS] \times C(Co)_T \tag{7}$$

2.4. Assessments of catalyst activity

The DBT HDS experiments were performed with a fixed-bed flow microreactor using a mixture of DBT (1.0 wt%) and decahydronaphthalene (as solvent). Before evaluation, all the catalysts were presulfided with a mixture of CS_2 (3.0 wt%) and *n*-heptane at 4.0 MPa and 360 °C for 4 h. The assessment pressure and temperature were 4.0 MPa and 340 °C, the liquid hourly space velocity (LHSV) was 15.0 h^{-1}, and the H_2/feed ratio was 400. Finnigan Trace chromatograph-mass spectrometer was used to analyzing the liquid products of DBT HDS.

Assuming the DBT HDS reaction followed a pseudo-first-order kinetic model, the reaction rate constant k_{HDS} (mol·g^{-1} ·s^{-1}) was obtained from the following equation (Hensen et al., 2001):

$$k_{HDS} = \frac{F}{m} \ln \frac{1}{1-x} \tag{8}$$

where F is the feed rate of DBT (mol·s^{-1}), m is the weight of the catalyst (g) and x is the DBT conversion (%).

HDS turnover frequencies (TOF, s^{-1}) for DBT were obtained by the following equation (Hensen et al., 2001):

$$TOF = \frac{F \cdot x}{n_{Mo} \cdot D} \tag{9}$$

where D is the MoS_2 particle dispersion and n_{Mo} is the content of Mo species in the catalyst (mol).

Based on reaction pathway for DBT HDS, the selectivity factor ($S_{DDS/HYD}$) for the direct desulfurization pathway (DDS) and the prehydrogenation pathway (HYD) was calculated by the following equation (Gao et al., 2015):

$$S_{DDS/HYD} = \frac{W_{BP}}{W_{CHB} + W_{TH} + W_{HH}} \tag{10}$$

where W_{TH}, W_{HH}, W_{CHB} and W_{BP} are respectively the contents (wt%) of tetrahydro-dibenzothiophene (THDBT), hexahydro-dibenzothiophene (HHDBT), cyclohexylbenzene (CHB) and biphenyl (BP) among the DBT HDS products.

3. Results and discussion

3.1. Characterizations of the sulfided Mo−H-x catalysts

3.1.1. XRD and N₂ adsorption-desorption

XRD results for the sulfided Mo−H-*x* (*x* = 0.1, 0.2, 0.3 and 0.5) catalysts in Fig. 1 indicated that the diffraction peaks at 14.0°, 33.2° and 58.6° corresponded well to the (002), (100) and (110) crystal planes of MoS_2 (JCPDS card no. 37−1492). The XRD patterns for all of the Mo−H-*x* catalysts showed only MoS_2 diffraction peaks and no other diffraction peaks, indicating that these catalysts were pure. After H_2O_2 etching, the diffraction peaks for the Mo−H-*x* catalysts were similar, which illustrated that H_2O_2 etching neither changed the crystalline structure of the MoS_2. Furthermore, with increasing H_2O_2 concentration, the (002) peak of the sulfided Mo−H-*x* catalysts shifted to a lower angle, demonstrating that the interlayer spacings of the MoS_2 slabs increased gradually. The increased interlayer spacing originated from weaker van der Waals interactions between MoS_2 slabs due to crystal defects (Guo et al., 2015). With increasing H_2O_2 concentration, the (100) peak of the sulfided Mo−H-*x* catalysts shifted to a higher angle because lattice distortions and stacking faults affected the MoS_2 lattice (Xie et al., 2013). In addition, the N_2 adsorption-desorption isotherms of Mo−H-*x* catalysts were presented in Fig. S1 and the results were summarized in Table S1. The results in Table S1 indicated that the BET specific surface areas and pore volumes of the Mo−H-*x* catalysts showed negligible changes as the H_2O_2 concentration was increased.

3.1.2. HRTEM

The SEM images for sulfided Mo−H-*x* are displayed in Fig. S2. The morphologies and structures of the MoS_2 catalysts were further characterized by HRTEM. As illustrated in Fig. 2, the sulfided Mo−H-*x* (*x* = 0, 0.1, 0.2 and 0.3) catalysts consisted of nanoflowers with light edges and dark centers, indicating that the MoS_2 morphology remained unchanged after low-concentration H_2O_2 etching ($\leq$ 0.3 mol/L). However, when the H_2O_2 concentration was increased from 0.3 to 0.5 mol/L, the sulfided Mo−H-0.5 catalyst showed a broken flower-like morphology. As shown in Fig. 3(b) and (h), the MoS_2 layer spacing increased from 0.62 to 0.65 nm, which resulted from introduction of defect sites such as aberrations, layer
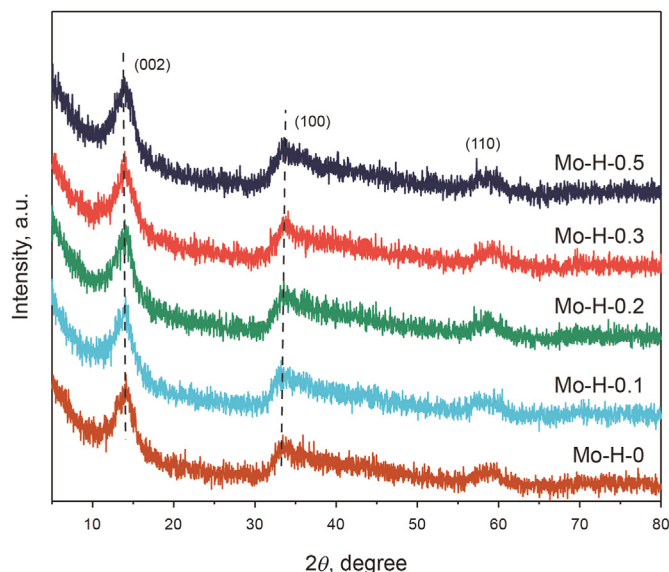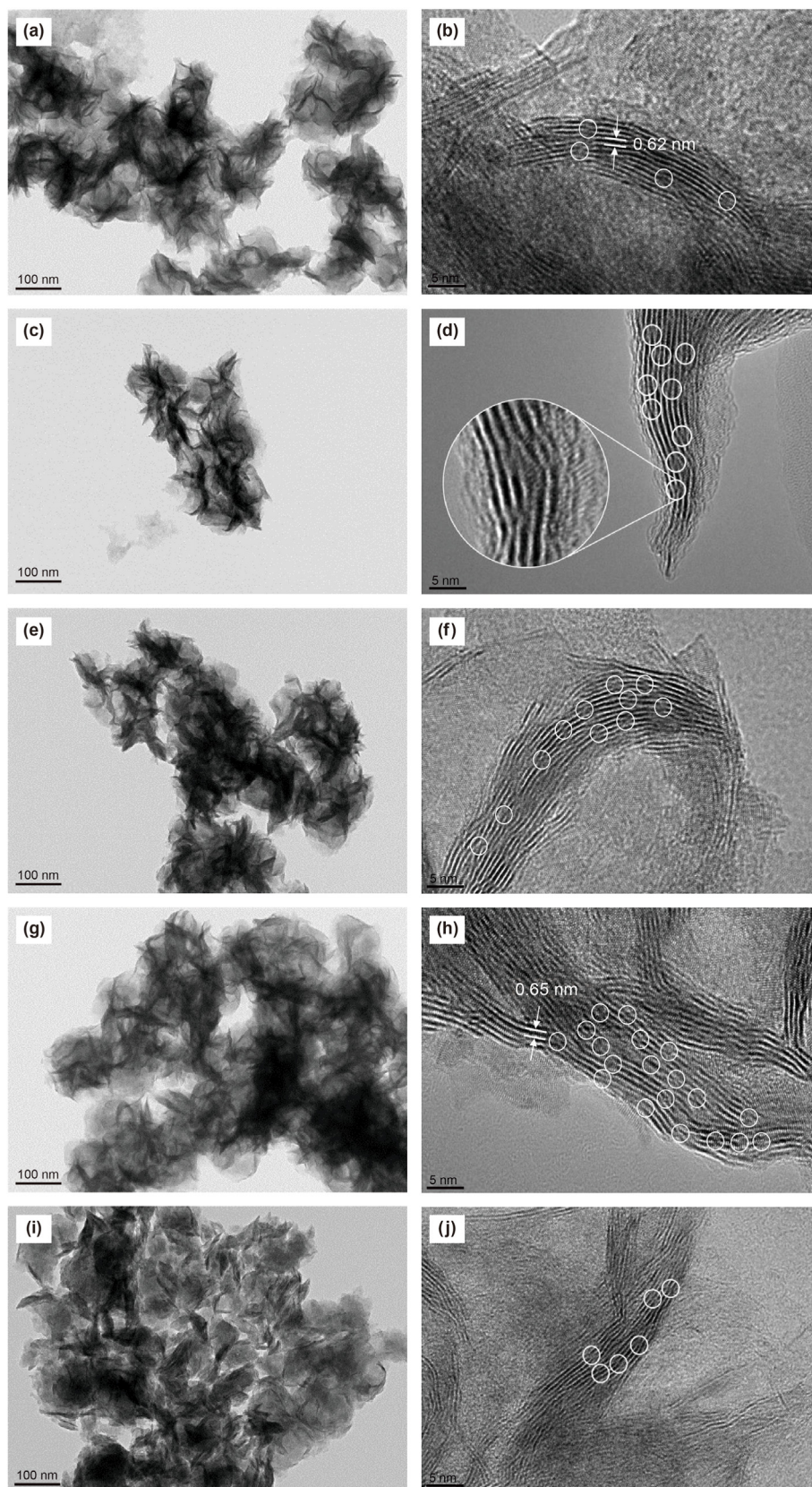

Fig. 1. XRD patterns of sulfided Mo−H-*x* catalysts.

Fig. 2. HRTEM images of sulfided Mo−H-*x*: Mo−H-0 (**a, b**), Mo−H-0.1 (**c, d**), Mo−H-0.2 (**e, f**), Mo−H-0.3 (**g, h**) and Mo−H-0.5 (**i, j**).
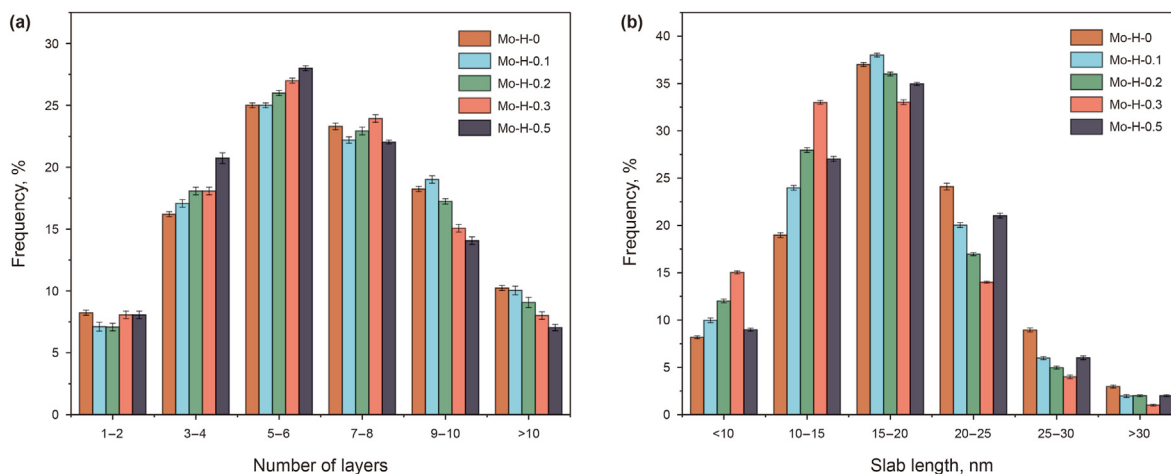
Fig. 3. Distributions of the length (**a**) and the layer number of MoS_2 slabs (**b**) on sulfided Mo−H-x catalysts.

dislocations and vacancies in the MoS_2 slabs caused by H_2O_2 etching. With increasing H_2O_2 concentration (0.1−0.5 mol/L), the number of defect sites at MoS_2 edges (white circle position in Fig. 3(b), (d), (f), (h) and (j)) first increased and then decreased, and the maximum value was obtained with 0.3 mol/L H_2O_2.

The lengths and stacking numbers of MoS_2 slabs are depicted in Fig. 3. The lengths of MoS_2 slabs in the sulfided Mo−H-x catalysts were predominantly distributed within the range 11−20 nm, and the numbers of stacking layers were mainly distributed within 5−8 layers. The results in Table 1 show that as the H_2O_2 concentration was increased, the average length of the MoS_2 slabs first decreased and then increased, the MoS_2 dispersion first increased and then decreased, and the average number of MoS_2 layers first remained at approximately 7.0 and then decreased. These results are explained as follows. When the MoS_2 slabs were exposed to low H_2O_2 concentrations (0.1−0.3 mol/L), some lattice defect sites formed on MoS_2 slabs crossed the (002) crystal plane, which divided the long MoS_2 lattice strips into several short strips and thereby shortened the MoS_2 length in the direction of the (002) crystal plane. Moreover, etching with low H_2O_2 concentrations had a negligible effect on the number of stacking layers. However, when the MoS_2 slabs were exposed to a high H_2O_2 concentration (0.5 mol/L), the average stacking number of MoS_2 was reduced by approximately one layer compared to etching with low H_2O_2 concentrations, which resulted from massive two-dimensional defect structures on the MoS_2 surface produced by the high-concentration H_2O_2 etching.

3.1.3. XPS

XPS analysis was conducted to determine the chemical compositions of the sulfided Mo−H-x surfaces. The binding energy difference for Mo $3d_{3/2}$ and Mo $3d_{5/2}$ was approximately 3.2 eV, and the relative area ratio was approximately 2:3. The Mo 3d spectra and the corresponding peak fitting results for sulfided Mo−H-x are presented in Fig. 4. There were three types of Mo chemical species
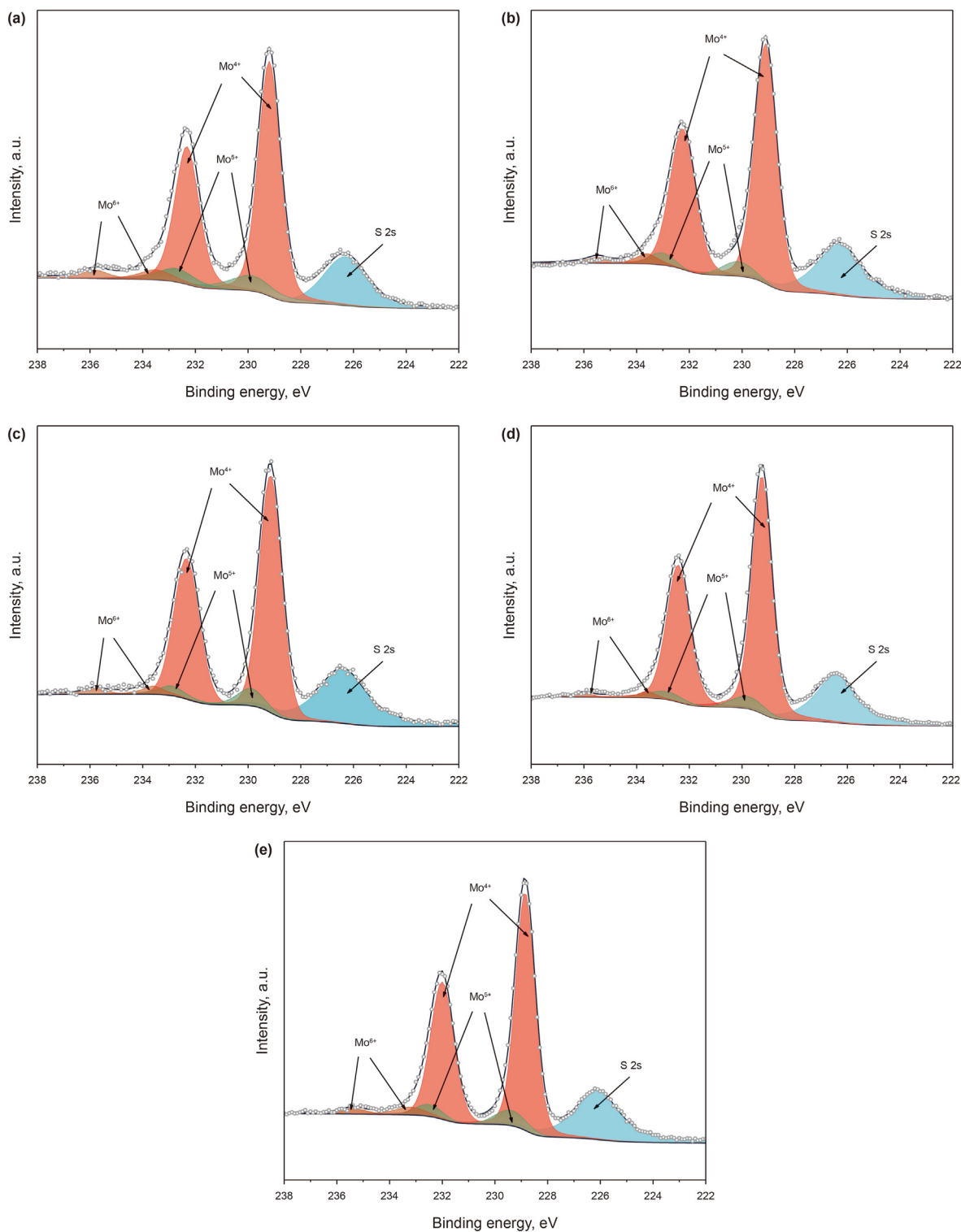
Table 1
Average length, average layer numbers and dispersion of MoS_2 slabs on sulfided Mo−H-x catalysts.

Catalyst	$\overline{L}$, nm	$\overline{N}$	D
Mo−H-0	18.4	7.0	0.061
Mo−H-0.1	17.5	7.1	0.066
Mo−H-0.2	16.1	7.0	0.069
Mo−H-0.3	14.5	6.8	0.075
Mo−H-0.5	17.8	6.0	0.064

existed on the catalyst surface: Mo^{4+}, Mo^{5+}, and Mo^{6+} related with MoS_2, MoO_xS_y oxysulfides and MoO_3, respectively; the corresponding banding energies were 229.1 ± 0.1, 229.9 ± 0.1 and 233.7 ± 0.1 eV, respectively. The S 2s binding energy was 226.2 ± 0.1 eV (Ninh et al., 2011). The peak fitting results in Table 2 show that the $Mo_{sulfurization}$ values for the sulfided Mo−H-x catalysts increased and then decreased as the concentration of the H_2O_2 solution was increased and reached a maximum at Mo−H-0.3. The positions of the Mo^{4+} binding energy peaks for Mo−H-0.1, Mo−H-0.2 and Mo−H-0.3 remained unchanged, which indicated that low-concentration H_2O_2 etching had a negligible effect on the surface structures of the Mo species. However, the Mo $3d_{3/2}$ and Mo $3d_{5/2}$ binding energy peaks attributed to Mo^{4+} in the sulfided Mo−H-0.5 catalyst shifted to lower energies by 0.3 eV, which indicated that the electronic structure of MoS_2 in the sulfided Mo−H-0.5 catalyst was changed by high-concentration H_2O_2 etching, resulting in shifts of the Mo 3d binding energy peaks (Li et al., 2019).

3.1.4. H₂-TPR

The obtained H_2-TPR results for the sulfided Mo−H-x catalysts are presented in Fig. 5. The reduction peaks observed for bulk MoS_2 catalysts below 300 °C were attributed to the reduction of weakly bonded S^{2-} species on the surface of MoS_2 particles (Yoosuk et al., 2008). When the MoS_2 surface was reduced by hydrogen, the CUS were generated, which were considered active sites for HDS (Varakin et al., 2018; Nag et al., 1980). The formed CUS numbers were determined by the amount of hydrogen consumption (Varakin et al., 2018; Nag et al., 1980). Mangnus et al. (1995) and Scheffer et al. (1990) indicated that the first H_2S evolution peak in the H_2-TPR patterns of MoS_2 based catalysts was assigned to reduction of S_x species adsorbed on coordinatively unsaturated (CUS) edge/corner sites that would be responsible for the HDS activity. Thus, the H_2 consumption amounts are equal to the numbers of coordinatively unsaturated sites. The H_2-TPR results in Table 3 show that all of the sulfided Mo−H-x catalysts exhibited low-temperature reduction peaks at approximately 235 °C, indicating that the effect of H_2O_2 etching on the Mo−S bond strength was negligible. When the H_2O_2 concentration was less than 0.3 mol/L, the amount of hydrogen consumption for sulfided Mo−H-x gradually increased with increasing H_2O_2 concentrations, which indicated that the number of active sites in sulfided Mo−H-x progressively increased. However, when the H_2O_2 concentration was further increased from 0.3 to 0.5 mol/L, the amount of hydrogen consumption decreased. This was because the contents of

Fig. 4. Mo 3d XPS spectra of sulfided Mo−H-*x*: Mo−H-0 (**a**), Mo−H-0.1 (**b**), Mo−H-0.2 (**c**), Mo−H-0.3 (**d**) and Mo−H-0.5 (**e**).

MoO_xS_y and MoO_3 species increased but the MoS_2 content decreased in sulfided Mo−H-0.5 compared to those in sulfided Mo−H-0.3 (Table 3), which lead to a decrease in the weakly bonded S^{2-} species for sulfided Mo−H-0.5.

3.1.5. EPR spectra

EPR spectroscopy is a powerful tool for studying chemical species with unpaired electrons or surface defects in the case of MoS_2. As shown in Fig. 6, all of the sulfided Mo−H-*x* catalysts exhibited a significant paramagnetic signal at approximately $g = 2.004$, which indicated the presence of dangling Mo−S bonds in Mo−H-*x* (Cao et al., 2020). In addition, the peak intensity is proportional to the concentration of Mo−S dangling bonds generated by coordinatively unsaturated S^{2-} species in MoS_2 slabs (Lei et al.,

Table 2
Fitting results of Mo 3d XPS on sulfided Mo−H-x catalysts.

Catalyst	Mo^{4+} 3d$_{5/2}$, eV	Mo^{4+} 3d$_{3/2}$, eV	Mo^{4+} phase, %[a]	Mo^{5+} phase, %	Mo^{6+} phase, %
Mo−H-0	229.1	232.3	80.0	13.5	6.5
Mo−H-0.1	229.1	232.3	84.6	11.2	4.2
Mo−H-0.2	229.1	232.3	88.0	9.2	2.8
Mo−H-0.3	229.1	232.3	91.9	6.0	2.1
Mo−H-0.5	228.8	232.0	83.2	12.4	4.4

[a] Mo$_{sulfurization}$ = Mo^{4+}/(Mo^{4+}+Mo^{5+}+Mo^{6+})
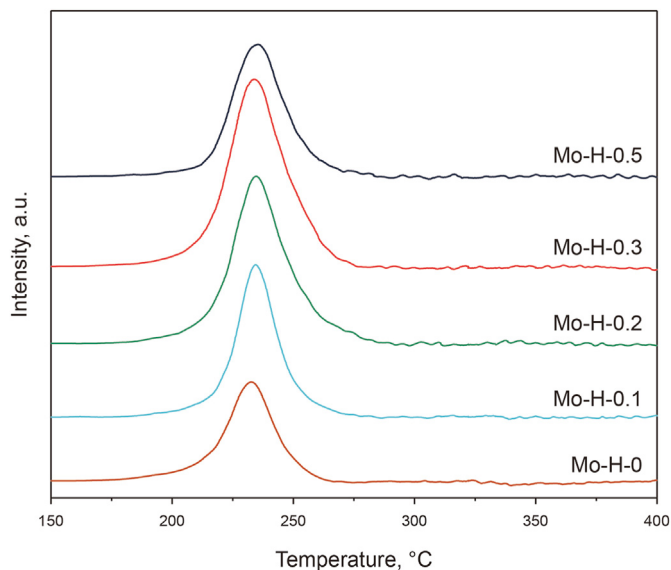
Fig. 5. H$_2$-TPR patterns of sulfided Mo−H-x catalysts.

Fig. 6. EPR spectra of sulfided Mo−H-x catalysts.

Table 3
Temperatures and H$_2$ consumptions of the low-temperature reduction peaks on sulfided Mo−H-x catalysts.
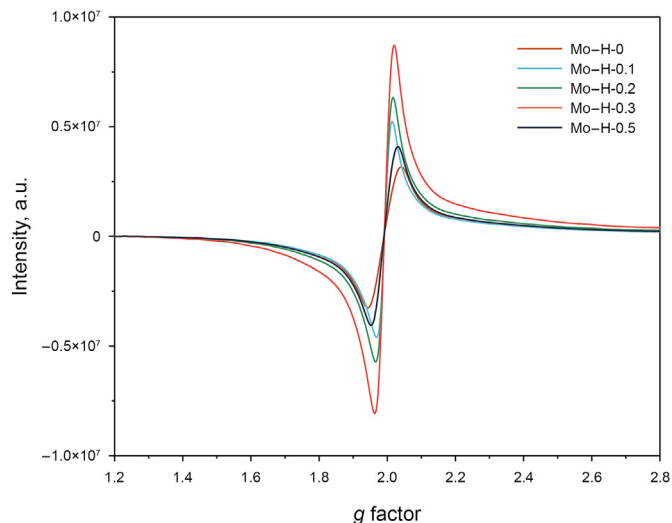
Catalyst	Peak temperature, °C	H$_2$ consumption, μmol·g^{-1}
Mo−H-0	234	6.5
Mo−H-0.1	235	9.9
Mo−H-0.2	235	13.8
Mo−H-0.3	234	16.7
Mo−H-0.5	235	8.8

2014). The peak intensities for sulfided Mo−H-x decreased in the order Mo−H-0.3 > Mo−H-0.2 > Mo−H-0.1 > Mo−H-0.5 > Mo−H-0, indicating that the coordinatively unsaturated S^{2-} content in sulfided Mo−H-x first increased and then decreased as the H$_2$O$_2$ concentration was increased, and a maximum was observed for sulfided Mo−H-0.3. The peak intensity of sulfided Mo−H-0.5 was lower than that of sulfided Mo−H-0.3 because etching with the high H$_2$O$_2$ concentration generated massive two-dimensional defect structures on MoS$_2$ slabs (Table 1), which led to the less Mo−S dangling bonds in sulfided Mo−H-0.5 than in sulfided Mo−H-0.3.

3.2. Characterizations of the sulfided x-CoMo catalysts

3.2.1. XRD

XRD patterns for the sulfide x-CoMo catalysts are shown in Fig. 7. All x-CoMo catalysts exhibited characteristic peaks at $2\theta = 14.0°$, 33.2° and 58.6°, which represented the MoS$_2$ crystalline phase (JCPDS 37−1492), and 0.2-CoMo and 0.3-CoMo also showed characteristic peaks attributed to Co$_9$S$_8$ at 29.8° and 52.1° (JCPDS 65−6801) (Liu et al., 2022). These results indicated that some cobalt species formed Co$_9$S$_8$ crystallites during sulfidation when the Co/(Co + Mo) ratio was greater than 0.2. In addition, the peak intensities for MoS$_2$ decreased with increasing Co loading (Liu et al., 2017). For the 0.05-CoMo and 0.1-CoMo catalysts, no diffraction peak was observed for Co$_9$S$_8$ in the XRD patterns. A weak diffraction peak for Co$_9$S$_8$ appeared in the pattern for 0.2-CoMo, indicating that a small amount of Co$_9$S$_8$ crystallites were formed in 0.2-CoMo. Furthermore, a strong diffraction peak for Co$_9$S$_8$ appeared in the pattern of 0.3-CoMo, which demonstrated that a large number of Co$_9$S$_8$ crystallites were formed in this catalyst.

3.2.2. XPS

The decompositions of Mo 3d core level in the sulfided x-CoMo catalysts are further investigated (Fig. 8). The relative proportions of Mo^{4+} in sulfided x-CoMo were approximately constant, consistent with that for the Mo−H-0.3 catalyst (Table 4). This result illustrated that the Co loading had a negligible effect on the proportion of Mo^{4+} in x-CoMo, which was beneficial for investigating the synergistic effects between Co species and MoS$_2$.

Fig. 9 shows the deconvolution results for the Co 2p spectra of sulfided x-CoMo. There were three types of Co chemical species existed on the catalyst surface, Co$_9$S$_8$, CoMoS, and CoO, and the corresponding banding energies were 793.3 ± 0.1 , 793.9 ± 0.1 and 798.7 ± 0.1 eV (Gandubert et al., 2006). The contents of different Co species on sulfided x-CoMo are listed in Table 4. A large proportion of the cobalt in 0.05-CoMo existed as CoMoS active phases, with only a trace amount of the Co$_9$S$_8$ phase detected on the catalyst surface. When the Co/(Co + Mo) ratio was increased from 0.05 to 0.1, the effective contents of the corresponding CoMoS active phases increased from 0.851 wt% on 0.05-CoMo to 1.855 wt% on
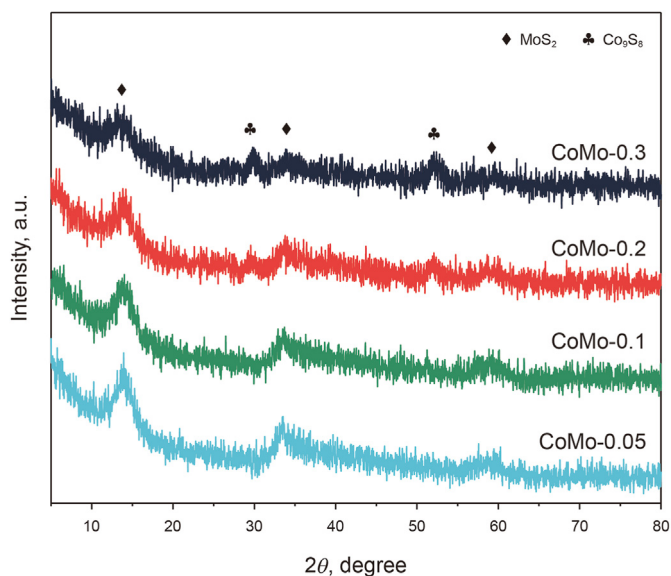
Fig. 7. XRD patterns of sulfided *x*-CoMo catalysts.

0.1-CoMo, indicating that the increase in Co loading generated more of the CoMoS active phase. Similarly, the 0.2-CoMo catalyst exhibited a higher content of CoMoS active phase than 0.1-CoMo. However, as the Co/(Co + Mo) ratio was increased from 0.2 to 0.3, the effective content of the CoMoS active phase decreased, and the effective content of the Co_9S_8 phase increased significantly. This meant that an overly high Co/(Co + Mo) ratio produced a high content of Co_9S_8, which covered the CoMoS active phases and thereby reduced the activity of CoMoS.

3.3. Catalytic activities of the sulfided Mo−H-x and x-CoMo catalysts

The activities of the sulfided Mo−H-*x* and *x*-CoMo catalysts were evaluated with DBT HDS tests. There are two reaction pathways for DBT desulfurization: the direct hydrodesulfurization pathway (DDS) and the prehydrodesulfurization pathway (HYD). For the DDS pathway, the C−S bonds of DBT are directly broken via hydrogenolysis to remove the sulfur atom and yield BP. In the HYD pathway, one of the aromatic rings in the DBT molecule is hydrogenated to form THDBT and HHDBT, followed by removal of the S atom to form CHB and BCH (Tuxen et al., 2012; Huirache-Acuña
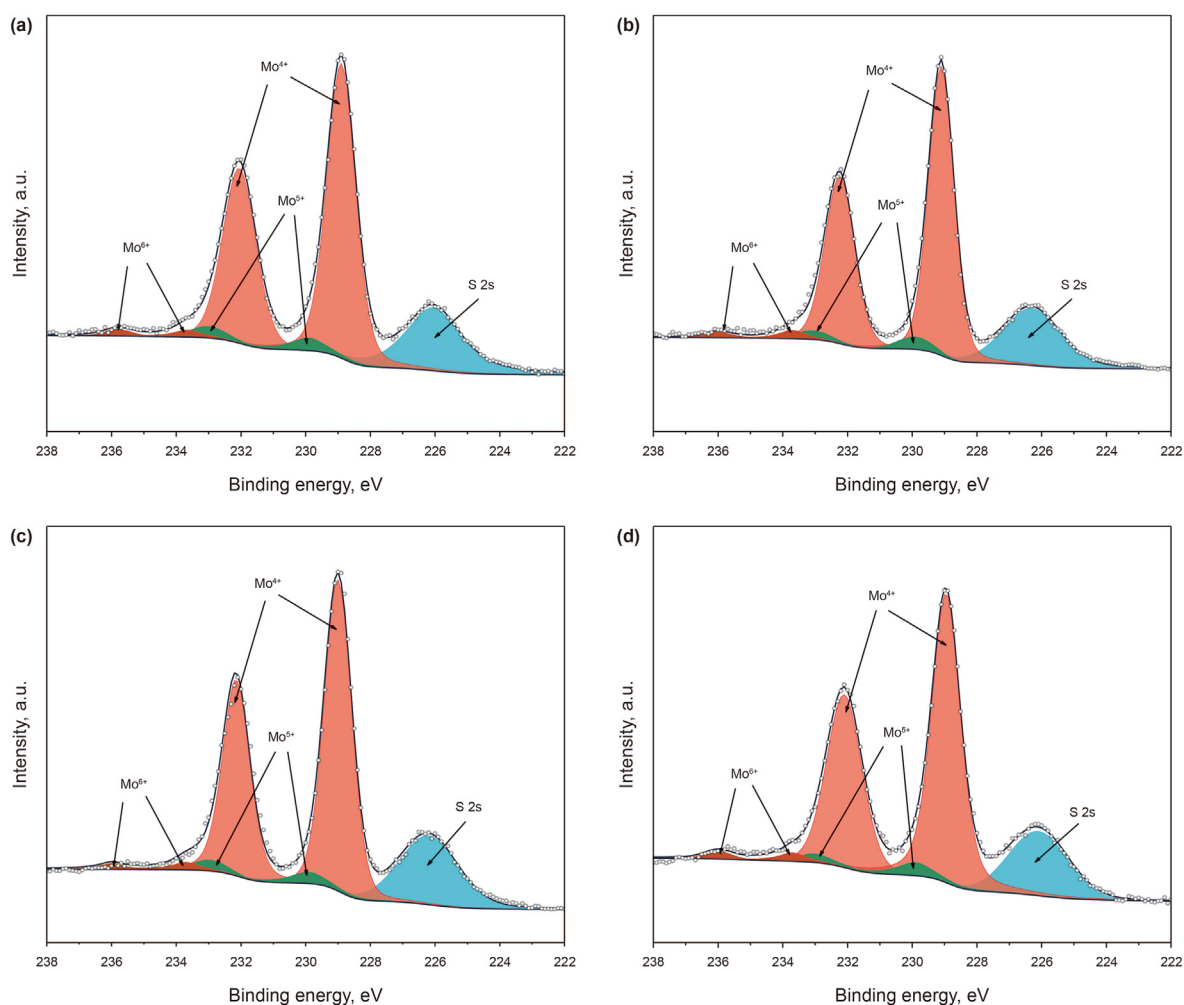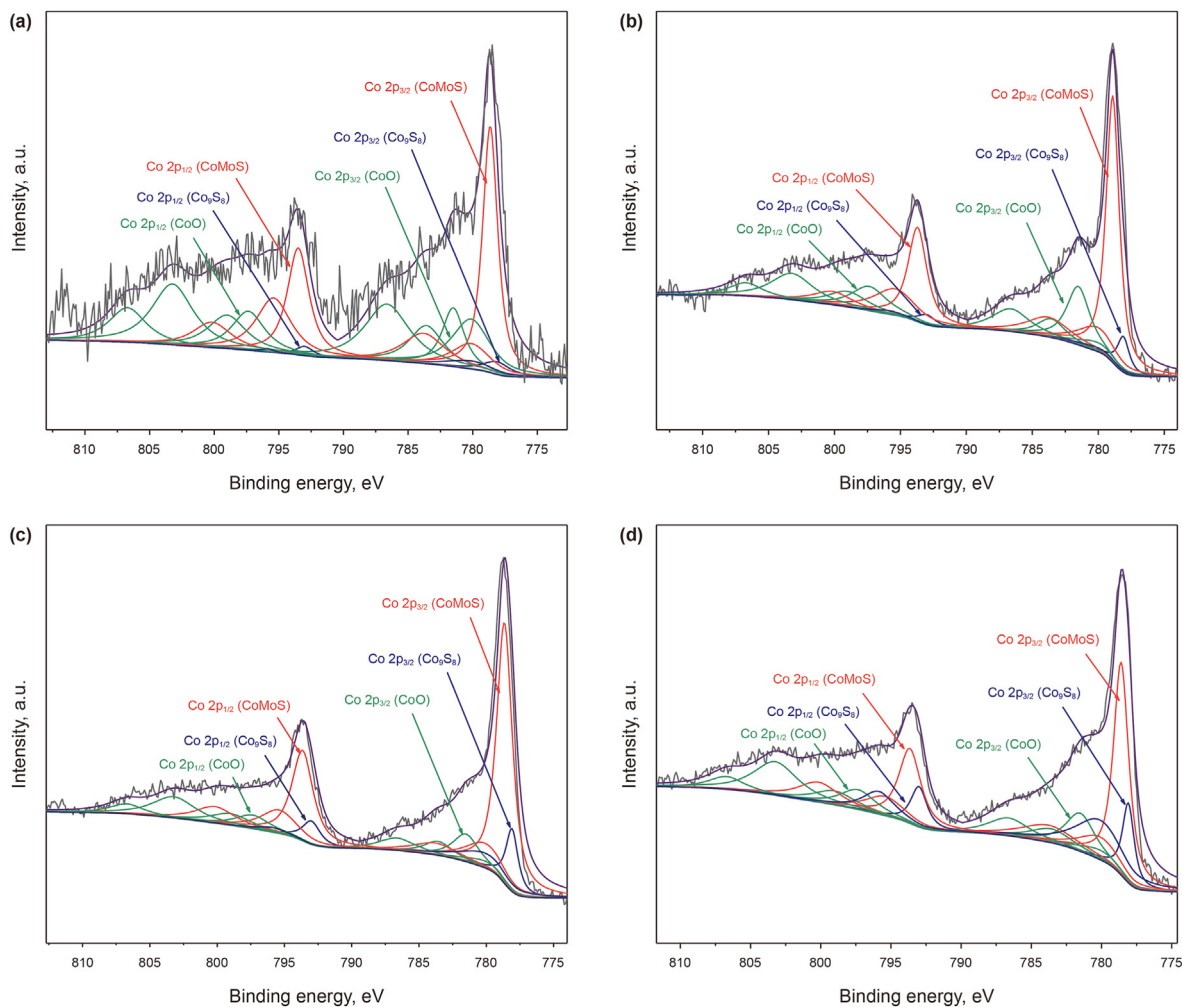

Fig. 8. Mo 3d XPS spectra of sulfided *x*-CoMo: 0.05-CoMo (**a**), 0.1-CoMo (**b**), 0.2-CoMo (**c**) and 0.3-CoMo (**d**).

Table 4
Fitting results of XPS spectra on sulfided *x*-CoMo catalysts.

Catalyst	Mo distribution, rel.%			Co distribution, rel.%			$C_{Co_9S_8}$ [a], wt%	C_{CoMoS} [a], wt%
	Mo^{4+}	Mo^{5+}	Mo^{6+}	CoMoS	Co_9S_8	CoO		
0.05-CoMo	91.8	5.5	2.7	49.3	3.6	47.1	0.062	0.851
0.1-CoMo	91.2	5.7	3.1	59.8	6.4	33.8	0.198	1.855
0.2-CoMo	91.5	5.4	3.1	62.9	12.6	24.5	0.769	3.853
0.3-CoMo	91.0	5.8	3.2	46.7	21.9	31.4	1.641	3.492

[a] Effective content of Co_9S_8 and CoMoS obtained by XPS.

Fig. 9. Co 2p XPS spectra of sulfided *x*-CoMo: 0.05-CoMo (**a**), 0.1-CoMo (**b**), 0.2-CoMo (**c**) and 0.3-CoMo (**d**).

Table 5
HDS results of DBT on the sulfided catalysts.

Catalyst	TOF[a], 10^{-4} s^{-1}	k_{HDS}[b], 10^{-6} mol^{-1} g^{-1} s^{-1}	S_{DDS}[c], %	S_{HYD}[c], %	$S_{DDS/HYD}$
Mo−H-0	0.47	0.25	58.3	41.7	1.40
Mo−H-0.1	1.28	1.09	61.2	38.8	1.58
Mo−H-0.2	2.05	1.93	65.6	34.4	1.91
Mo−H-0.3	2.84	2.75	68.7	31.3	2.19
Mo−H-0.5	1.09	0.86	60.4	39.6	1.53
0.05-CoMo	3.25	3.84	74.2	25.8	2.88
0.1-CoMo	4.67	4.76	79.4	20.6	3.85
0.2-CoMo	7.64	6.95	81.5	18.5	4.41
0.3-CoMo	6.39	5.78	71.4	28.6	2.50

[a] Number of reacted DBT molecules per second and per Mo atom at the edge surface.
[b] Calculated at about 25% of DBT conversion.
[c] Calculated according to the final products in DBT HDS at about 25% of DBT conversion.

et al., 2015). The selectivity factors ($S_{DDS/HYD}$) at approximately 25% DBT conversion were greater than 1 for all nine catalysts (Table 5), which indicated that DBT was mainly desulfurized via the DDS pathway. For the sulfided Mo−H-*x* catalysts, the k_{HDS} and TOF values decreased in the order Mo−H-0.3 > Mo−H-0.2 > Mo−H-0.1 > Mo−H-0.5 > Mo−H-0, which demonstrated that the Mo−H-0.3 catalyst had the highest k_{HDS} and TOF values. Introduction of Co into the monometallic molybdenum catalyst (Mo−H-0.3) significantly improved the HDS activity of the catalyst, and the corresponding k_{HDS} and TOF values for the bimetallic *x*-CoMo catalysts decreased in the order 0.2-CoMo > 0.3-CoMo > 0.1-CoMo > 0.05-CoMo. In Table 6, the k_{HDS} value of the optimal 0.2-CoMo catalyst was compared with those of reported Co−Mo HDS catalysts, and the results indicated that 0.2-CoMo had the highest k_{HDS} value among these catalysts. The results of stability tests for DBT HDS on Mo−H-0.3 showed that the DBT HDS ratio of this catalyst remained stable at 94.4% during test for 133 h, which indicated the good stability of Mo−H-0.3 during DBT HDS (Fig. S3).

3.4. Microstructure-activity correlations for sulfided Mo−H-x and x-CoMo

3.4.1. Correlation of CUS concentration with HDS activity based on sulfided Mo−H-x

The relationship between the CUS concentration (C_{CUS}) and the HDS rate constant (k_{HDS}) are shown in Fig. 10. The k_{HDS} value increased linearly with increasing C_{CUS} value, and the highest k_{HDS} was obtained with Mo−H-0.3. The Mo−H-0 catalyst without H_2O_2 etching showed the lowest C_{CUS} value, which resulted in the lowest k_{HDS}. For Mo−H-*x* (*x* = 0.1, 0.2 and 0.3), the exfoliating effect of H_2O_2 on S atoms was gradually enhanced as the H_2O_2 concentration was increased (0.1−0.3 mol/L); the relatively integral edges of MoS_2 slabs were continuously etched when H_2O_2 reacted with S and Mo atoms, which increased the "perimeter" of the MoS_2 slab and was equivalent to reducing the horizontal sizes of the MoS_2 slabs (Zhang et al., 2019). Thus, the etched MoS_2 slabs exposed more unsaturated S^{2-} sites. Consequently, the C_{CUS} values increased gradually with increasing H_2O_2 concentration, and thereby, the k_{HDS} for Mo−H-0.1, Mo−H-0.2 and Mo−H-0.3 increased successively. However, when the H_2O_2 concentration was increased from 0.3 to 0.5 mol/L, the C_{CUS} value decreased, and the k_{HDS} value for Mo−H-0.5 decreased. This was because more MoO_xS_y and MoO_3 species in sulfided Mo−H-0.5 than in sulfided Mo−H-0.3 (Table 2) reduced the number of unsaturated S^{2-} sites in the former catalyst. Hence, Mo−H-0.3, which had the highest CUS concentration, showed the best DBT HDS performance among the Mo−H-*x* catalysts.

3.4.2. Correlations of the effective contents of CoMoS with HDS activity based on sulfided x-CoMo

It is commonly believed that introduction of cobalt into Mo-based catalysts significantly enhances their HDS performance (Okamoto et al., 1977; Payen et al., 1994). The promoting effect of cobalt on MoS_2 catalysis was dominated by electronic contributions, and donation of electrons from Co to Mo weakened the strengths of Mo−S bonds, which increased the number of CoMoS active phases and thereby enhanced the HDS activity (Berhault
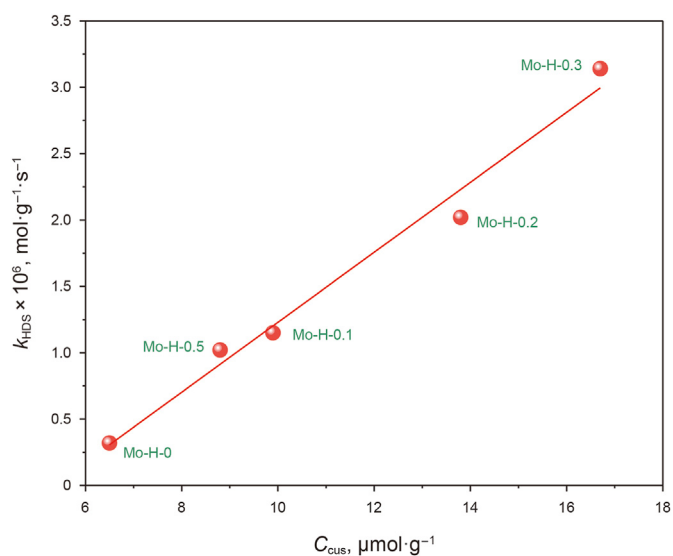

Fig. 10. Correlations between k_{HDS} and the CUS concentrations obtained from H_2 consumption amounts in H_2-TPR.

et al., 2008). Thus, the HDS performance of a CoMo catalyst depended on the effective content of CoMoS active phases (C_{CoMoS}). The relationships of effective CoMoS with the HDS activities of the *x*-CoMo catalysts are presented in Fig. 11. The k_{HDS} increased linearly with increasing in C_{CoMoS}. For increasing Co/(Co + Mo) ratios of *x*-CoMo, the C_{CoMoS} value first increased and then decreased and showed a maximum value for 0.2-CoMo. When the Co/(Co + Mo) ratio was less than 2.0, the C_{CoMoS} values for *x*-CoMo gradually increased with increasing Co loading. However, when the Co/
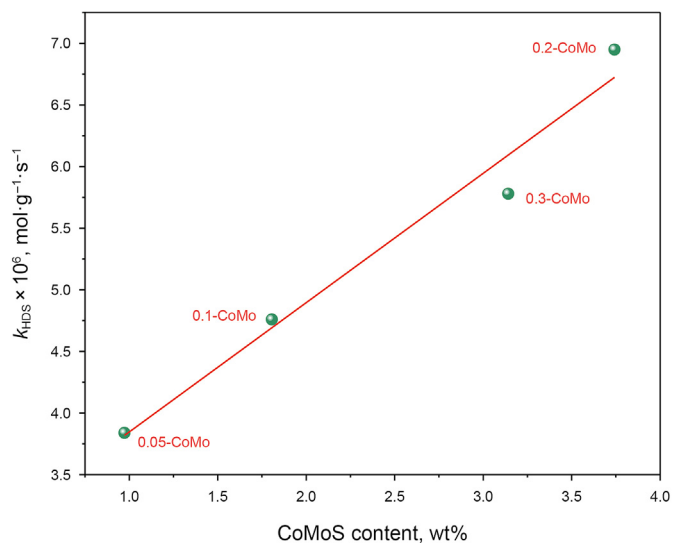

Fig. 11. Correlations between the effective CoMoS content and k_{HDS}.

Table 6
Comparisons of k_{HDS} values between the 0.2-CoMo catalyst and the reported HDS catalysts for the HDS of DBT.

Catalyst	Conditions	k_{HDS}, 10^{-6} mol^{-1} g^{-1} s^{-1}	Ref.
0.2-CoMo	T = 340 °C, P = 4.0 MPa	6.95	This work
CoMoW−H	T = 350 °C, P = 3.1 MPa	2.0	Huirache-Acuña et al. (2006)
La$_{0.25}$Co$_{0.75}$MoS$_2$	T = 350 °C, P = 1.2 MPa	1.07	Valdes et al. (2021)
CoMo/Al (10) KIT-6	T = 320 °C, P = 5.5 MPa	0.87	Suresh et al. (2017)

(Co + Mo) ratio was greater than 0.2, the excess Co_9S_8 phases covered some of the CoMoS active phases, which resulted in a lower C_{CoMoS} value for 0.3-CoMo; thus, the k_{HDS} of 0.3-CoMo was less than that of 0.2-CoMo. The above analyses demonstrated that the 0.2-CoMo catalyst with the highest CoMoS content exhibited superior performance for DBT HDS among x-CoMo catalysts.

4. Conclusions

A H_2O_2 etching strategy was proposed to introduce coordinatively unsaturated sites (CUS) in three-dimensional MoS_2 nanoflowers synthesized for DBT HDS. This method finely modulated the CUS concentrations on MoS_2 slabs by varying the H_2O_2 concentrations. The exfoliating effect of H_2O_2 on the S atoms was gradually enhanced as the H_2O_2 concentration was increased (0.1–0.3 mol/L), and the etched MoS_2 slabs possessed more unsaturated S^{2-} sites. However, when the MoS_2 slabs were exposed to a high H_2O_2 concentration (0.5 mol/L), more MoO_xS_y and MoO_3 species in the sulfided Mo–H-0.5 catalyst than in the sulfided Mo–H-0.3 catalyst decreased the number of unsaturated S^{2-} sites in Mo–H-0.5. Thus, the CUS concentration in Mo–H-0.5 was less than that of Mo–H-0.3. The correlation between the etched MoS_2 microstructure and the HDS activity showed that more CUS introduced on MoS_2 slabs effectively promoted DBT HDS. Therefore, the Mo–H-0.3 catalyst with the highest CUS concentration showed the highest k_{HDS} value (2.75×10^{-6} mol g^{-1} s^{-1}) among the Mo–H-x catalysts. Furthermore, different Co loadings were introduced into Mo–H-0.3, and the resulting 0.2-CoMo catalyst with the highest CoMoS content (3.853 wt%) exhibited the highest reaction rate constant, 6.95×10^{-6} mol g^{-1} s^{-1}, among these bimetallic CoMo catalysts. Compared with reported Co–Mo HDS catalysts, the optimal 0.2-CoMo catalyst in this work had a higher reaction rate constant, shedding a light on the development of high-performance HDS catalysts.

Declaration of competing interest

The authors declare that they have no known competing financial interests or personal relationships that could have appeared to influence the work reported in this paper.

Acknowledgments

Appendix A. Supplementary data

Supplementary data to this article can be found online at https://doi.org/10.1016/j.petsci.2023.08.002.

References

Abbasi, A., Karimi, A., Aghabozorg, H., et al., 2020. Cobalt-promoted MoS_2 nanosheets: a promising novel diesel hydrodesulfurization catalyst. Int. J. Chem. Kinet. 52, 159–166. https://doi.org/10.1002/kin.21338.

Afanasiev, P., 2010. The influence of reducing and sulfiding conditions on the properties of unsupported MoS_2-based catalysts. J. Catal. 269, 269–280. https://doi.org/10.1016/j.jcat.2009.11.004.

Asadi, A.A., Royaee, S.J., Alavi, S.M., et al., 2019. Ultra-deep hydrodesulfurization of cracked and atmospheric gasoil blend: direct and interactive impacts of support composition, chelating agent, metal and promoter loadings. Fuel Process. Technol. 187, 36–51. https://doi.org/10.1016/j.fuproc.2019.01.007.

Berhault, G., De la Rosa, M.P., Mehta, A., et al., 2008. The single-layered morphology of supported MoS_2-based catalysts-The role of the cobalt promoter and its effects in the hydrodesulfurization of dibenzothiophene. Appl. Catal., A: Gen. 345, 80–88. https://doi.org/10.1016/j.apcata.2008.04.034.

Brunet, S., Mey, D., Perot, G., et al., 2005. On the hydrodesulfurization of FCC gasoline: a review. Appl. Catal., A: Gen. 278, 143–172. https://doi.org/10.1016/j.apcata.2004.10.012.

Cao, H., Bai, Z., Li, Y., et al., 2020. Solvothermal synthesis of defect-rich mixed 1T-2H MoS_2 nanoflowers for enhanced hydrodesulfurization. Acs. Sustain. Chem. Eng. 8, 7343–7352. https://doi.org/10.1021/acssuschemeng.0c00736.

Chowdari, R.K., Leon, J.N.d., Fuentes-Moyado, S., 2021. Template-free, facile synthesis of nickel promoted multi-walled MoS_2 & nano-bricks containing hierarchical MoS_2 nanotubes from the bulk NiMo oxide. Appl. Catal. B Environ. 298, 120617. https://doi.org/10.1016/j.apcatb.2021.120617.

De la Rosa, M.P., Texier, S., Berhault, G., et al., 2004. Structural studies of catalytically stabilized model and industrial-supported hydrodesulfurization catalysts. J. Catal. 225, 288–299. https://doi.org/10.1016/j.jcat.2004.03.039.

Feng, L.p., Su, J., Li, D.p., et al., 2015. Tuning the electronic properties of Ti-MoS_2 contacts through introducing vacancies in monolayer MoS_2. Phys. Chem. Chem. Phys. 17, 6700–6704. https://doi.org/10.1039/c5cp00008d.

Gandubert, A.D., Legens, C., Guillaume, D., et al., 2006. X-ray photoelectron spectroscopy surface quantification of sulfided CoMoP catalysts. Relation between activity and promoted sites. Part II: influence of the sulfidation temperature. Surf. Interface Anal. 38, 206–209. https://doi.org/10.1002/sia.2249.

Gao, D., Duan, A., Zhang, X., et al., 2015. Synthesis of NiMo catalysts supported on mesoporous Al-SBA-15 with different morphologies and their catalytic performance of DBT HDS. Appl. Catal. B Environ. 165, 269–284. https://doi.org/10.1016/j.apcatb.2014.10.034.

Guo, J., Li, F., Sun, Y., et al., 2015. Oxygen-incorporated MoS_2 ultrathin nanosheets grown on graphene for efficient electrochemical hydrogen evolution. J. Power Sources 291, 195–200. https://doi.org/10.1016/j.jpowsour.2015.05.034.

Hensen, E.J.M., Kooyman, P.J., van der Meer, Y., et al., 2001. The relation between morphology and hydrotreating activity for supported MoS_2 particles. J. Catal. 199, 224–235. https://doi.org/10.1006/jcat.2000.3158.

Huirache-Acuña, R., Albiter, M.A., Ornelas, C., et al., 2006. Ni(Co)-Mo-W sulphide unsupported HDS catalysts by ex situ decomposition of alkylthiomolybdotungstates. Appl. Catal., A: Gen. 308, 134–142. https://doi.org/10.1016/j.apcata.2006.04.015.

Huirache-Acuña, R., Zepeda, T.A., Rivera-Munoz, E.M., et al., 2015. Characterization and HDS performance of sulfided CoMoW catalysts supported on mesoporous Al-SBA-16 substrates. Fuel 149, 149–161. https://doi.org/10.1016/j.fuel.2014.08.045.

Kasztelan, S., Toulhoat, H., Grimblot, J., et al., 1984. A geometrical model of the active phase of hydrotreating catalysts. Appl. Catal. 13, 127–159. https://doi.org/10.1016/S0166-9834(00)83333-3.

Lai, W., Chen, Z., Zhu, J., et al., 2016. A NiMoS flower-like structure with self-assembled nanosheets as high-performance hydrodesulfurization catalysts. Nanoscale 8, 3823–3833. https://doi.org/10.1039/c5nr08841k.

Lei, F., Sun, Y., Liu, K., et al., 2014. Oxygen vacancies confined in ultrathin indium oxide porous aheets for promoted visible-light water splitting. J. Am. Chem. Soc. 136, 6826–6829. https://doi.org/10.1021/ja501866r.

Li, L., Qin, Z., Ries, L., et al., 2019. Role of sulfur vacancies and undercoordinated Mo regions in MoS_2 nanosheets toward the evolution of hydrogen. ACS Nano 13, 6824–6834. https://doi.org/10.1021/acsnano.9b01583.

Li, Q., Hu, B., Yang, Q., et al., 2020. Interaction mechanism between multi-layered MoS_2 and H_2O_2 for self-generation of reactive oxygen species. Environ. Res. 191, 110227. https://doi.org/10.1016/j.envres.2020.110227.

Li, Y., Li, A., Li, F., et al., 2014. Application of HF etching in a HRTEM study of supported MoS_2 catalysts. J. Catal. 317, 240–252. https://doi.org/10.1016/j.jcat.2014.06.007.

Liu, B., Liu, L., Wang, Z., et al., 2017. Effect of hydrogen spillover in selective hydrodesulfurization of FCC gasoline over the CoMo catalyst. Catal. Today 282, 214–221. https://doi.org/10.1016/j.cattod.2016.08.020.

Liu, M., Wang, L., Yu, X., et al., 2022. Introducing oxygen vacancies for improving the electrochemical performance of Co_9S_8@NiCo-LDH nanotube arrays in flexible all-solid battery-capacitor hybrid supercapacitors. Energy 238, 121767. https://doi.org/10.1016/j.energy.2021.121767.

Mangnus, P.J., Riezebos, A., Vanlangeveld, A.D., et al., 1995. Temperature-programmed reduction and HDS activity of sulfided transition metal catalysts: formation of nonstoichiometric sulfur. J. Catal. 151, 178–191. https://doi.org/10.1006/jcat.1995.1020.

Nag, N.K., Fraenkel, D., Moulijn, J.A., et al., 1980. Characterization of hydroprocessing catalysts by resolved temperature-programmed desorption, reduction and sulfiding. J. Catal. 66, 162–170. https://doi.org/10.1016/0021-9517(80)90018-4.

Nikulshin, P.A., Ishutenko, D.I., Mozhaev, A.A., et al., 2014. Effects of composition and morphology of active phase of CoMo/Al_2O_3 catalysts prepared using Co_2Mo_{10}-heteropolyacid and chelating agents on their catalytic properties in HDS and HYD reactions. J. Catal. 312, 152–169. https://doi.org/10.1016/j.jcat.2014.01.014.

Ninh, T.K.T., Massin, L., Laurenti, D., et al., 2011. A new approach in the evaluation of the support effect for NiMo hydrodesulfurization catalysts. Appl. Catal., A: Gen. 407, 29–39. https://doi.org/10.1016/j.apcata.2011.08.019.

Okamoto, Y., Nakano, H., Shimokawa, T., et al., 1977. Stabilization effect of Co for Mo phase in CoMo/Al_2O_3 hydrodesulfurization catalysts studied with X-ray photoelectron spectroscopy. J. Catal. 50, 447–454. https://doi.org/10.1016/0021-9517(77)90057-4.

Payen, E., Hubaut, R., Kasztelan, S., et al., 1994. Morphology study of MoS_2 and WS_2 based hydrotreating catalysts by high-resolution electron microscopy. J. Catal. 147, 123–132. https://doi.org/10.1006/jcat.1994.1122.

Pimerzin, A.A., Ishutenko, D.I., Mozhaev, A.V., et al., 2017. Comparable investigation of spillover and cobalt promoter effects in CoMoS/CoS$_x$/SiO$_2$ catalysts for selective hydrotreating of model FCC gasoline. Fuel Process. Technol. 156, 98−106. https://doi.org/10.1016/j.fuproc.2016.10.023.

Scheffer, B., Dekker, N., Mangnus, P., et al., 1990. A temperature-programmed reduction study of sulfided CoMo/Al$_2$O$_3$ hydrodesulfurization catalysts. J. Catal. 121, 31−46. https://doi.org/10.1016/0021-9517(90)90214-5.

Song, W., Lai, W., Chen, Z., et al., 2018. Fabrication of 3D porous hierarchical NiMoS flowerlike architectures for hydrodesulfurization applications. ACS Appl. Nano Mater. 1, 442−454. https://doi.org/10.1021/acsanm.7b00299.

Suresh, C., Perez-Cabrera, L., Diaz de Leon, J.N., et al., 2017. Highly active CoMo/Al (10) KIT-6 catalysts for HDS of DBT: role of structure and aluminum heteroatom in the support matrix. Catal. Today 296, 214−218. https://doi.org/10.1016/j.cattod.2017.04.048.

Tuxen, A.K., Fuchtbauer, H.G., Temel, B., et al., 2012. Atomic-scale insight into adsorption of sterically hindered dibenzothiophenes on MoS$_2$ and Co-Mo-S hydrotreating catalysts. J. Catal. 295, 146−154. https://doi.org/10.1016/j.jcat.2012.08.004.

Valdes, C., Gonzalez, D., Flores, K., et al., 2021. Effect of Lanthanum Doping on the reactivity of unsupported CoMoS$_2$ catalysts. Appl. Catal., A: Gen. 611. https://doi.org/10.1016/j.apcata.2020.117891.

Varakin, A.N., Mozhaev, A.V., Pimerzin, A.A., et al., 2018. Comparable investigation of unsupported MoS$_2$ hydrodesulfurization catalysts prepared by different techniques: advantages of support leaching method. Appl. Catal. B Environ. 238, 498−508. https://doi.org/10.1016/j.apcatb.2018.04.003.

Wang, Z.G., Pei, J.N., Chen, S.L., et al., 2017. The surface properties of aluminated meso-macroporous silica and its catalytic performance as hydrodesulfurization catalyst support. Petrol. Sci. 14, 424−433. https://doi.org/10.1007/s12182-017-0150-9.

Xie, J., Zhang, H., Li, S., et al., 2013. Defect-rich MoS$_2$ ultrathin nanosheets with additional active edge sites for enhanced electrocatalytic hydrogen evolution. Adv. Mater. 25, 5807−5813. https://doi.org/10.1002/adma.201302685.

Xiong, Q.l., Zhang, J., Xiao, C., et al., 2017. Effects of atomic vacancies and temperature on the tensile properties of single-walled MoS$_2$ nanotubes. Phys. Chem. Chem. Phys. 19, 19948−19958. https://doi.org/10.1039/c7cp02667f.

Yoosuk, B., Kim, J.H., Song, C., et al., 2008. Highly active MoS$_2$, CoMoS$_2$ and NiMoS$_2$ unsupported catalysts prepared by hydrothermal synthesis for hydrodesulfurization of 4,6-dimethyldibenzothiophene. Catal. Today 130, 14−23. https://doi.org/10.1016/j.cattod.2007.07.003.

Yuan, P., Lei, X.Q., Sun, H.M., et al., 2020. Effects of pore size, mesostructure and aluminum modification on FDU-12 supported NiMo catalysts for hydrodesulfurization. Petrol. Sci. 17, 1737−1751. https://doi.org/10.1007/s12182-020-00502-5.

Zhang, B., Xiang, H., Tao, L., et al., 2019. Chemically activated MoS$_2$ for efficient hydrogen production. Nano Energy 57, 535−541. https://doi.org/10.1016/j.nanoen.2018.12.045.

Zhou, W., Liu, M., Zhou, Y., et al., 2017. 4,6-dimethyldibenzothiophene hydrodesulfurization on nickel-modified USY-supported NiMoS catalysts: effects of modification method. Energy Fuels 31, 7445−7455. https://doi.org/10.1021/acs.energyfuels.7b01113.